Relations between microstructure, precipitation, age-formability and damage tolerance of Al-Cu-Mg-Li (Mn,Zr,Sc) alloys for age forming

M.J. Starink, N. Gao[*], N. Kamp[a], S.C. Wang, P.D. Pitcher[b], I. Sinclair

Materials Research Group, School of Engineering Sciences,
University of Southampton, Southampton, SO17 1BJ, UK
[a] currently at Manchester Materials Science Centre, UMIST, Manchester M1 7HS, UK
[b] QinetiQ, Farnborough GU14 OLX, UK

Abstract

Age forming of Al based alloys for damage tolerant applications requires an alloy with good age formability and good post-forming mechanical properties. To investigate optimisation of this balance, several newly designed Al-Cu-Mg-Li (Mn,Zr,Sc) alloys were subjected to artificial ageing representative of age-forming. It was seen that combinations of yield strength and fatigue crack growth resistance could be achieved that are at least comparable to the incumbent damage tolerant material for such applications, whilst creep rates at the ageing temperatures applied were better than those achieved in commercially applied age forming processes of heat treatable Al based alloys. Coarse grain structure and high Li content are associated with good fatigue crack growth resistance but reduce age formability. The underlying physical aspects responsible for the balance between creep rates and resulting properties are discussed. The metallurgical and micromechanical mechanisms analysed and discussed provide a framework for optimisation of composition and forming conditions for age forming of damage tolerant parts.

Keywords: Age forming; 2xxx alloys; Fatigue resistance; Grain size; Toughness

1. Introduction

In age forming of aluminium alloys for airframe applications, curved wing skin components are manufactured by mechanically conforming a plate or sheet over a specially designed curved tool, with the metal and tool combination then being held (under load) at the alloy's ageing temperature to simultaneously achieve precipitation in the alloy and creep relaxation of the material into the required curvature [1,2]. After release of the load springback will occur, which can be substantial. The process offers considerable design and manufacturing benefits over conventional forming operations such as peen forming, bump pressing and roll forming, through high potential of automation, potential of increased component accuracy and reduced residual stress levels. The process is directly amenable to higher strength 7xxx alloy components, as these are already

---

[*] Corresponding author. Tel.: +44-238-059-3396; Fax: +44-238-059-3016
E-mail address: n.gao@soton.ac.uk (N. Gao)

optimised for use in artificially aged tempers [2,3], and the process is becoming established in airplane upper wing applications where 7xxx alloys are typically employed. However, incumbent lower wing skin alloys, such the 2024 Al-Cu-Mg-Mn based alloys in the damage tolerant T351 condition, lose their critical damage tolerant properties upon ageing. The main challenge for application in these and other damage tolerant parts lies in obtaining the best balance between the often conflicting sets of requirements such as creep rate during age forming and fatigue crack growth resistance of the age formed product. A limited number of works have been published which focus on the principles of this relatively new processing technique [1,2] and on application to selected standard aerospace Al based alloys [3,4]. However, no reports on the main mechanisms responsible for the relations between composition, formability and resulting properties have been published, and no methodologies for optimising the combination of alloys and process with respect to damage tolerant properties have been published.

Li additions to Al-Cu(-Mg) alloys are known to have a beneficial influence on fatigue crack growth rate, whilst precipitation is modified by formation of δ' (Al$_3$Li) precipitates [5,6] and an expected change in rate of S phase precipitation [7]. Thus Li additions can significantly alter both the main properties and the thermomechanical processing required to obtain optimum properties. A group of potentially age formable alloys around the composition range Al-(2-4)Cu-(1-2)Mg-(0.2-1.6)Li (wt%) with Mn, Zr and/or Sc additions has been investigated. Extensive analysis of the microstructure [5,7] and mechanical properties [4,8], in combination with modelling of the composition-processing-property relations, was used in an iterative process in the development and optimisation of the alloys. Following the earlier work which focussed on microstructural analysis and modelling of strength or fatigue crack growth micromechanics, the main aim of the present paper is to analyse the physical aspects that are responsible for the balance between creep rate during age forming and the resulting mechanical properties. Thus the paper aims to elucidate the key aspect of alloy and process design for age forming of damage tolerant heat treatable Al based alloys. To this end, key results of the microstructure analysis and materials testing from this project are presented and the main property-formability balances are analysed. The main aspects of the modelling of these relationships are also discussed. The present paper is the first to present an analysis of the formability, micro and nanostructure development and resulting properties of a range of alloys specifically designed for age forming.

2. Alloy selection and property modelling

The combined requirements of good forming properties at typical age forming temperatures and good resulting (damage tolerant) mechanical properties, which is a new combination of requirements, requires the investigation of new alloy formulations. To aid this, processing-microstructure-properties models were developed and used together with existing models as aids for alloy design. An age hardening model has been developed to predict the yield strength of Al-Cu-Mg alloys with composition within the α+S phase field of the phase diagram [9,10]. To date a total of 16 alloys based mostly around the Al-Cu-Mg system have been designed; the present paper will focus on the alloys listed in Table 1. The composition of alloy 6 is close to the median composition of 2024. Compositions of alloys 3-4 and 7-10 are aimed to achieve a yield strength that does not

significantly exceed 2024-T351 yield strength as increasing yield strength is detrimental to toughness in aluminium alloys [11], whilst a high yield strength is also thought to reduce age formability, especially if the strength is caused by solution strengthening. The addition of Li in selected alloys was made to take advantage of the associated improved fatigue crack growth resistance but Li contents were limited to 1.6 wt% to limit formation of δ' (Al_3Li) precipitates which are associated with reduced toughness. An analytical model of roughness induced crack closure (RICC) has been developed to provide a semi-quantitative relation between fatigue crack growth (FCG) and microstructural features [12]. As underaged alloys generally show a better FCG resistance, alloy design aims at slowing down the precipitation process in these alloys compared to 2024. It was thought that this can be achieved by reduced Cu+Mg content and also by microalloying with Li and Zr (see Section 4.2 and 5).

3. Experimental procedures

Experimental alloys (Table 1) have been manufactured at QinetiQ, Farnborough, UK. Billets were conventionally cast, stress relieved, homogenized, hot rolled to 20 mm thickness, solution heat treated, cold water quenched and stretched by ~2.5%. Except for solution treatment temperatures, the processing was essentially the same for all alloys (optimum solution temperatures for individual alloys were identified via determination of the start temperature of (incipient) melting using differential scanning calorimetry (DSC) [13]). To simulate ageing during age forming, heat treatments at 150 and 190°C were performed.

Grain structure and crystallographic texture of the alloys was determined using electron backscatter diffraction (EBSD) on a Jeol JSM-6500 multi-purpose high performance field emission gun scanning electron microscope (FEG-SEM) (see e.g. [14]). EBSD data was analysed with the aid of HKL Channel 5 software. Tensile tests were carried out on an Instron machine with a cross head speed of 1 mm/min at room temperature.

The DSC experiments were conducted using a Perkin-Elmer Pyris 1 within the temperature range 5-540°C at a constant heating rate of 10°C/min. Disc-shaped samples were made with a thickness about 0.9 mm and diameter 5 mm. Baseline correction was performed in two stages. First a DSC run with empty pans was subtracted from the experiment. Secondly, the data was corrected by assuming the combined effect of heat capacity differences and baseline fluctuations results in a heat flow which is a second order polynomial [13]. The coefficients were fitted by assuming that the heat effects due to reactions are zero at three temperatures: 40, 120 and 498°C.

Thin foils for transmission electron microscopy (TEM) were prepared using a standard procedure: samples of 400 μm thickness were punched, ground to 250 μm and electro-polished using a 1/3 nitric acid, 2/3 methanol solution held at −20°C to −30°C, with a voltage of 25V. TEM observation was performed at 200kV using a Jeol JEM-2000FX.

Fatigue crack growth tests were carried out according to ASTM E-647 using compact tension specimens taken in the LT orientation. Tests were performed in air using a loading frequency of

20Hz and a stress ratio of 0.1. Age formability was assessed via creep tests conducted for 20h. Tests were conducted in tension with an applied stress of 150 MPa at 190°C.

Alloy	Cu	Mg	Zr	Mn	Sc	Li	Grain size (μm)
3	2.27	1.03	0.11	0.01	-	1.56	6
4	2.24	0.94	-	0.42	-	1.60	113
5	4.30	1.46	0.06	0.43	-	0.17	142
6	4.34	1.37	-	0.42	-	-	157
7	2.08	0.97	0.11	-	0.21	0.55	4
8	2.22	0.90	0.11	-	-	0.57	18
9	1.48	1.43	0.11	-	-	0.54	29
10	2.10	0.9	0.11	-	-	0.74	12

Table 1 Compositions and average grain size of the alloys studied (wt%)

4. Results

4.1. Grain structure

A wide range of microstructures was obtained in these alloys. The grain size of these alloys (as measured with the aid of EBSD) was determined mostly by the dispersoid forming element (see Table 1). The Mn-containing alloys 4, 5 and 6 were predominantly found to be recrystallized with coarse grains (113-157 μm), whilst the Zr-containing alloys (alloys 3, 8, 9, 10) were only partially recrystallized with smaller grain sizes (Fig. 1), with average grain size of 6 to 29 μm. A particularly fine grain structure (4 μm) was evident in the Zr and Sc containing alloy 7. The EBSD work carried on these alloys shows that all alloys have typical rolling and recrystallization textures. The Zr containing alloy 7 has strongest Goss texture (i.e. {110}<001>), which forms on rolling, whereas very weak Goss texture remains in the Mn containing alloys 4-6. This is due to the Sc containing dispersoids hinder recrystallization very effectively, whilst the Mn containing alloys are mostly recrystallized.

4.2. Precipitation

In terms of strengthening precipitates, a distinct difference was observed between alloys aged at 150°C and 190°C with the former containing predominantly clusters and the latter S phase. Three dimensional atom probe (3DAP) analysis on alloys 3, 4 and 6 was performed by Davin and co-workers [15,16] using an energy-compensated optical position sensitive atom probe. For all alloys studied by 3DAP Cu-Mg co-clusters were identified after ageing at 150ºC. For both of alloys 3 and 4 aged between 6 h and 12 h at 150ºC, the cluster density was shown to be stable within measurement accuracy but after 24h, the density increases sharply. The size of the clusters is similar for the three ageing conditions. The average composition of the clusters does not vary greatly with time [15]. In addition to the clusters, Cu/Mg-rich precipitates were observed. In the early stages these precipitates have a clear platelet shape and are only composed of a few atomic layers. After

12h at 150°C, the Cu/Mg-rich precipitates also possess a platelet shape but some of the precipitates seem to be formed by the merging of two rod-like precipitates (Fig. 2). Evidence of some δ' precipitates also was found in alloy 3 and 4 by TEM analysis, with $L1_2$ ordered composite β'(Al_3Zr)/δ' particles appearing in alloy 3 (Fig. 3) and precipitation of needle or lath-shaped S phase was observed in all the alloys at 190°C ageing (Fig. 4).

DSC experiments were performed for all alloys aged at 150 and 190°C. The basic shape of the DSC curves is similar for all alloys, revealing the heat effects due to zone/cluster dissolution (endothermic effect typically in the range 170-230°C), S formation (an exothermic precipitation effect occurs mostly between 230 and 300°C) and S dissolution (Fig. 5). The endothermic effect related to the dissolution of Cu/Mg containing clusters can also contain a contribution due to dissolution of δ' (Al_3Li) for alloys with Li contents higher than 1 wt%. Figure 5(a) shows that ageing at 150°C has caused the formation of clusters. A slight reduction in the S phase formation peak with the increase of ageing time observed at 150°C for most alloys indicates some S phase has started to form (Fig. 5(a)). Ageing at 190°C for 6 h causes the cluster dissolution effect to disappear, and the S phase formation effect reduces significantly in the same period (Fig. 5(b)). This is due to the formation of S phase at 190°C which consumes the clusters [9,17]. In order to investigate the influence of Li content on the rate of S phase formation, the peak temperature of S phase precipitation as observed in DSC experiments has been plotted against lithium content for alloys with Cu >1.5 wt%, in Fig. 6(a). It can be seen that an increase of lithium content results in an increase of S precipitation peak temperature which means that the S phase formation rate is slowed down by Li addition. Also the ratio of the heat content of the S phase formation effect after 190°C/6h and in T351 condition, r ($r = Q_{190°C/6h} / Q_{T351}$), is also plotted against lithium content (Fig. 6(b)). The data shows that the reduction of the S phase formation effect is enhanced with decreasing Li content. So also this figure indicates that the S phase formation rate is slowed down by Li addition. The reduction in S formation rate with Li addition may be ascribed to the reduced mobility of vacancies due to the formation of Li-vacancy pairs. The change of Zr content in these alloys has shown no significant effect on S precipitation temperature and formation rate.

4.3. Mechanical properties after simulated age forming

Alloys 5 and 6 possess a yield strength and ultimate tensile strength (UTS) that is significantly higher than 2024-T351 (tensile test results presented elsewhere [8]), but after ageing alloys 3, 4, 7 and 8 achieve tensile properties comparable or slightly better than 2024-T351. Alloys 9 and 10, with reduced Cu+Mg levels exhibit lower strengths. It should be noted that the strategy devised to slow down the precipitation process, i.e. reduced solute content and microalloying, has been successful as alloys 3, 4, 7, 8, 9 and 10 reach peak strength well after alloys 5 and 6 do. Measured yield strength results were generally in good agreement with expected yield strength from model predictions [9,10]. Comparison of tensile properties for specimens aged at 190°C and 150°C showed an increased yield strength of up to 100 MPa for the alloy aged at 190°C [8]. This means that alloys YS and UTS can be 'fine tuned' by adjusting the ageing treatment and/or composition to achieve the target strength properties. Results of the toughness ranking exercise also were obtained by plotting crack strength (i.e. toughness) against yield strength, which demonstrated that these

alloys have achieved the desired toughness level of 2024-T351 and indicated that toughness is not a limiting factor for the alloy design [8].

The FCG rates for alloys aged at 190°C for 12h are plotted in Fig. 7 together with typical upper and lower limits for 2024-T351. The FCG rates are plotted as a function of the nominal ΔK derived from the macroscopic loading of the samples (see e.g. [12]), thus allowing comparison of alloys that is relevant to the application. (For discussion of attenuation of ΔK due to micromechanical crack closure effects, see section 5.) All alloys, except alloy 7 aged at 190°C/12h, have FCG rates in the same range as 2024-T351 values obtained by Bray et al. [18]. At low ΔK, materials heat treated at 150°C/12h yielded slightly better FCG resistance than those aged at 190°C/12h. The influence of the grain structure was clearly seen: large, recrystallised grains in alloy 4 were seen to enhance fatigue performance compared to partially recrystallised grains in alloy 3. This is also highlighted by the relatively poor performance of alloy 7, which exhibits a very fine grain structure with the smallest grain size among all the alloys. Though the effect of Li is not explicitly separated because of the interactive effects of several alloying elements in the alloys and the typical scatter encountered in the crack growth rate data, a beneficial effect of increased Li content is identifiable.

4.4. Creep

Figure 8 shows the results of creep tests performed on alloys 3, 4, 5, 7 and 8 at 190°C at a stress of 150 MPa. Considering alloy 3, 4, 7 and 8, the creep performance seems to scale with the grain size. Alloy 7 which contains Sc and Zr has the finest grain size (see Fig. 1 and Table 1) and exhibits the fastest creep rate which means it has the best creep formability potential. Alloy 3 and 8 which are Zr-containing alloys, with fine grains (largely unrecrystallised), have lower creep rates than alloy 7 but higher creep rate than alloy 4 which contains large grains and is fully recrystallised (Mn-containing alloy). However, alloy 5 which is fully recrystallised and contains large grains, has creep properties similar to alloys 3 and 8, illustrating that parameters other than grain size may also have a strong influence on creep properties. A comparison of alloy 4 and 5, and alloy 3 and 8 suggest a detrimental effect of Li on creep rate/formability. In general the creep rates for the present underaged alloys are either comparable or better than the creep rates of other alloys used in commercial age forming operations (particularly 7xxx-series), and hence the present alloys can be considered to be age formable.

5. Discussion

The results show clear correlations between composition, microstructure and precipitation on the one hand and the creep rate and mechanical properties on the other and highlight the conflicting requirements for high creep rate and high FCG resistance. We will here analyse the mechanisms responsible for this balance, which is crucial for application of age forming to structures with high FCG resistance requirements. We will first consider the mechanisms involved in creep of the present alloys, and subsequently consider the dominant mechanism determining FCG resistance.

5.1. Mechanisms of Creep

Creep is generally ascribed to three mechanisms [19-22]. When bulk diffusion dominates, that is, when creep occurs by stress-directed flow of vacancies and diffusion occurs mainly through the crystal lattice, the creep is called Nabarro-Herring creep. The governing equation is:

$$\dot{\varepsilon}_{\mathrm{NH}} = A_{\mathrm{NH}} \frac{D_1}{d^2} \frac{\sigma\Omega}{kT} \tag{1}$$

However, when boundary diffusion dominates, it is known as Coble creep:

$$\dot{\varepsilon}_{\mathrm{C}} = A_{\mathrm{C}} \frac{\delta D_{\mathrm{GB}}}{d^3} \frac{\sigma\Omega}{kT} \tag{2}$$

where $\dot{\varepsilon}$ is the creep rate, A_{NH} and A_{C} are constants, D_1 and D_{GB} are the coefficient for lattice self-diffusion and grain boundary diffusion, respectively, Ω the atomic volume, σ the applied stress, d the grain size, T the temperature and k is Boltzmann's constant. δ is the effective width of the grain boundary for vacancy diffusion. Nabarro-Herring creep is usually dominant at high temperatures and Coble creep is dominant at about 0.4 T_{M} , where T_{M} is melting point of the material [23]. Both Nabarro-Herring and Coble creep are strongly grain size dependent and they are a linear-viscous processes. From the equations (1) and (2), it can be seen that at a given stress and temperature the creep rate increases with decreasing grain diameter. The ability of dislocations to climb at high temperatures introduces a third mechanism: dislocation creep [24,25]. The governing equation is:

$$\dot{\varepsilon}_{\mathrm{D}} = A_{\mathrm{D}} \frac{D_1 G b}{kT} \left(\frac{\sigma}{G}\right)^n \tag{3}$$

where A_{D} and n are constants, G is the shear modulus and b is the Burgers vector. Dislocation creep is independent of grain size and is a non-linear process. The creep behaviour of materials can also differ under different stress/temperature conditions. According to the 'deformation mechanism map' [23,25], creep in pure aluminium at the current stress levels and temperatures encountered in age forming is located close the boundary of in the dislocation creep and Coble creep regimes (just within the dislocation creep regime). Compared with pure aluminium dislocation movement in our alloys will be much reduced due to drag by solute atoms and the presence of dislocation pinning precipitates. This will cause the dislocation-creep field to shrink and the fields for diffusional creep mechanisms to expand [25]. Hence it is believed that the Coble creep mechanism is dominant for our alloys at the (simulated) age forming temperatures applied. This is supported by the experimental results (Fig. 8) which show a clear grain size effect on the creep rate, consistent with diffusional creep and inconsistent with dislocation creep. Also the reduction in creep rate with increasing Li content would be consistent with a diffusion creep mechanism, as Li-vacancy pairs will cause a reduction in vacancy mobility.

5.2. Mechanisms of fatigue crack growth resistance

Fatigue is a multifaceted physical/mechanical phenomenon for which no complete theory linking microstructure and micromechanical effects to crack growth is available. In damage tolerant aluminium based alloys one aspect that has been shown to have a strong influence on crack growth rates is the crack closure [26], especially roughness induced closure (RICC) [27,28], which is influenced by the deflection angles of crack segments and the characteristic length between deflected crack segments. These, in turn depend on the propensity for shear band formation, crystallographic texture and grain size. In recent work on experimental determination and micromechanical modelling, RICC shear strains causing asperity contact are considered to arise explicitly from residual plastic deformation in the wake of a propagating crack [12]. The crack closure and resulting reduction in K have been analysed both for a 2D situation (profile of crack is unchanged along the crack front direction) [12] and a 3D situation in which the crack surface has ridges both parallel and normal to the crack [29]. In the latter the model includes a 3 dimensional representation of the crack surface with mode II and mode III contributions to the crack closure, as illustrated in Fig 9, which also illustrates the surface parameters included in the model. The analytical model estimates the crack opening along an idealised deflected crack path and residual shear at each asperity interfering with this opening to generate closure. In this analysis closure is given by [29]:

For $a^* > \lambda r_p$:

$$\frac{K_{cl}}{K_{I\,max}} = \beta \frac{\sqrt{3\pi}K_{I\,max}\left(\frac{1}{2}+R-\frac{1}{2}R^2\right)}{2\sigma_0\sqrt{a^*}}\left[\frac{1}{2}\sin^2\frac{\theta}{2}\cos\frac{\theta}{2}\sin 2\theta + \frac{[1-2\nu]^2}{(1-\nu)}\sin^3\Phi\cos^2\Phi\frac{\sin\frac{\theta}{2}}{\cos^2\frac{\theta}{2}}\right] \qquad (4)$$

For $a^* < \lambda r_p$:

$$\frac{K_{cl}}{K_{I\,max}} = \beta \frac{\sqrt{3\pi a^*}K_{I\,max}\left(\frac{1}{2}+R-\frac{1}{2}R^2\right)}{2\sigma_0\lambda r_p}\left[\frac{1}{2}\sin^2\frac{\theta}{2}\cos\frac{\theta}{2}\sin 2\theta + \frac{[1-2\nu]^2}{(1-\nu)}\sin^3\Phi\cos^2\Phi\frac{\sin\frac{\theta}{2}}{\cos^2\frac{\theta}{2}}\right] \quad (5)$$

where a^* is the crack propagation distance since the last asperity tip, R is the load ratio (minimum over maximum applied stress), σ_o is the yield strength, r_p is the plastic zone size, ν is the Poisson ratio, θ and Φ are the angles defining the deflections parallel to crack growth direction and crack front, respectively, and λ and β are fitting parameters (linked to the physical length scales of plastic deformation at the crack tip), FE modelling suggests a reasonable value for λ to be the order of 0.4 [12]. In the 2D analysis closure is given by:

$$\frac{K_{cl}}{K_{I\,max}} = \beta \frac{\sqrt{3\pi}K_{I\,max}\left(\frac{1}{2}+R-\frac{1}{2}R^2\right)\left(\sin\frac{\theta}{2}+\sin\frac{3\theta}{2}\right)^2\sin 2\theta}{16\sigma_0\sqrt{a^*}\left(3\cos\frac{\theta}{2}+\cos\frac{3\theta}{2}\right)} \qquad (6)$$

8

A full analysis shows that crack closure levels rise monotonically with asperity sizes, and hence grain size, although these effects saturate when asperity size significantly exceeds the active plastic zone size, and a detailed analysis of relations between grain size, surface roughness and FCG resistance was presented elsewhere [12]. The reduction in FCG resistance with increasing ageing temperature can be understood within the context of these crack closure models, as S phase formed at higher ageing temperatures (Fig. 5) will cause dispersion of slip and thus result in less faceting and reduced roughness of the surface, whilst the increase in strength will reduce plastic deformation at the tip. Thus, in the window of ageing treatments studied here, the observed replacement of the shearable co-clusters by S phase with increasing time and temperature is the main cause for reduction of FCG resistance, with RICC being the micromechanical mechanism responsible. This RICC was further investigated by determining the variation of the crack closure levels with varying ΔK using a curve fitting method [27] for the alloys aged at 190°C/12h. Consistent with the present analysis, the results show that the alloy with smallest grain size (alloy 7) has the least closure effect, whilst the alloy with largest grain size (alloy 4) has the largest closure effect. Alloy 4 in particular is characterized by a combination of the highest Li content and large grain size: both factors may be expected to cause increasing slip heterogeneity. The relationships between surface roughness, closure levels and FCG performance were further investigated and confirmed by qualitative assessment of the fracture surfaces using 3D Talysurf profilometry, which clearly showed that the higher closure observed in the alloys with coarse grains (such as alloy 4) is associated with rougher fracture surfaces [29].

5.3. Balance of formability and damage tolerance

The age forming temperature will strongly influence the balances between creep and FCG resistance and between creep and yield strength. The present results have shown that the yield strength after (simulated) age forming can be readily manipulated through adjusting the level of alloying elements, and resulting strength can be predicted using strength models. In terms of the balance between creep and FCG resistance, Fig. 10 shows the relationship between creep strain and crack growth rate at $\Delta K = 7$ MPa m$^{1/2}$ for alloys with Cu content larger than 1.5 wt%. This figure shows that increase of creep (increasing the creep formability) is related to a reduced FCG resistance.

The reduction in FCG resistance on ageing is caused by the thermally activated process of S phase formation which consumes the clusters/zones present in underaged conditions, and the resulting reduced slip heterogeneity and RICC is a key factor. Thus both the increase in creep rate and the reduction in FCG resistance with increasing forming temperature are promoted by diffusion processes, in the former it is the diffusion of vacancies along grain boundaries due to Coble creep and in the latter it is the diffusion of Cu and Mg atoms, which in turn will depend on the diffusion of vacancies, which assist diffusion of the alloying elements. If one process, e.g. vacancy diffusion, governs both precipitation and creep, then the attainment of a particular level of creep would result in a fixed amount of precipitation, independent of (small) changes in the ageing temperature. In other words: for each alloy and for a range of ageing temperatures and times, the relation between amount of creep relaxation and FGR at a characteristic ΔK would be a single monotonously decreasing function. Thus manipulation of the ageing temperature may not lead to identification of

9

an optimum ageing temperature and it should be expected that the balance of creep and FCG resistance can not be significantly altered by changing forming temperature within 150-190°C. This indicates that optimisation should be sought through optimising alloy composition and grain structure.

The above discussion reveals the fundamental physical processes responsible for the conflicting requirements for high creep rate and high FCG resistance. The wider results obtained show that it is possible to balance the two requirements and that after artificial ageing simulating age forming the 3 main properties (yield strength, FCG resistance and toughness) of several of the new alloys are at least comparable 2024-T351. Thus there is a clear potential for damage tolerant age-formed structures using newly defined alloys. The metallurgical and micromechanical mechanisms analysed and discussed in this work provide a framework for optimisation of composition and forming conditions for age forming of damage tolerant parts.

6. Conclusions

1. On basis of processing-microstructure-properties models, several alloys potentially suitable for age forming were designed. A group of potentially age formable alloys around the composition range Al-(2-4)Cu-(1-2)Mg-(0.2-1.6)Li (wt%), with Mn, Zr and/or Sc additions has been investigated. Microstructural changes during age forming is simulated by heat treatments at 150 and 190°C, and formability is tested by creep tests at 190°C.

2. The grain structure in these alloys is mostly determined by Mn, Zr and Sc additions. Precipitation in all alloys relevant for age forming is dominated by cluster formation (150°C) and S phase formation (190°C). The addition of lithium in the alloys delays S precipitation during ageing.

3. Fatigue properties of these alloys after simulated age forming are similar or slightly better than 2024-T351. FCG resistance reduces on increasing the ageing temperature from 150 to 190°C. Extrinsic contributions to fatigue resistance have been identified with roughness induced crack closure processes. These alloys showed reasonable basic potential for creep forming and high creep rates were associated with small grain size.

4. An analysis of creep data suggests that grain boundary (Coble) creep is the dominant mechanism in creep relaxation during age forming. Vacancy mobility enhances Coble creep, which will benefit the forming process, but also enhances the rate of degradation of FCG resistance through enhanced precipitation rates. The models for Coble creep and for crack closure demonstrate that grain size has conflicting impact on creep rate (formability) and FCG resistance.

References

[1] K.C. Ho, J. Lin, T.A. Dean, J. Mater. Processing Technol. 153-154 (2004) 122.

[2] M.C. Holman, J. Mechanical Working Tech. 20 (1989) 477.

[3] P.D. Pitcher, C.M. Styles, Mater Sci Forum 331-333 (2000) 455.

[4] N. Gao, L. Davin, S. Wang, A. Cerezo, M.J. Starink, Mater Sci Forum 396-402 (2002) 923.

[5] N. Gao, M.J. Starink, L. Davin, A. Cerezo, S. Wang, P.J. Gregson, Mater Sci Techn. 21 (2005) 1010.

[6] S.C. Wang, M.J. Starink, Int Mater Rev 50 (2005) 193.

[7] M.J. Starink, I. Sinclair, N. Gao, N. Kamp, P.J. Gregson, P.D. Pitcher, A. Levers, S. Gardiner, Mater Sci Forum 396-402 (2002) 601.

[8] N. Kamp, M.J. Starink, I. Sinclair, N. Gao, P.J. Gregson, P.D. Pitcher, S. Gardiner, In: J.F. Nie, A.J. Morton, B.C. Muddle (Eds.), Proc. ICAA9, Aug. 2-5, 2004, Brisbane, Australia, Inst. of Mater. Eng. Australasia Ltd, p. 369.

[9] M.J. Starink, J. Yan, In: M. Tiryakioglu, L.A. Lalli (Eds.), Proc. 1st Int. Symposium on Metall. Modelling for Aluminium Alloys, Pittsburgh, PA, USA, ASM International, 2003. p.119.

[10] M.J. Starink, N. Gao, L. Davin, J. Yan, A. Cerezo, Phil Mag. 85 (2005) 1395.

[11] N. Kamp, I. Sinclair, M.J. Starink, Metall Mater Trans 33 (2002) 1125.

[12] N. Kamp, M.R. Parry, D.S. Singh, I. Sinclair, Acta Mater 52 (2003) 343.

[13] M.J. Starink, Int Mater Rev 49 (2004) 191.

[14] M.J. Starink, S.C. Wang, Acta Mater 51 (2003) 5131.

[15] L. Davin, A. Cerezo, N. Gao, M.J. Starink, Surf. Interface Analysis 36 (2004) 589.

[16] L. Davin, PhD thesis, Oxford University, Oxford, U.K., 2004.

[17] S.C. Wang, M.J. Starink, N. Gao, Scripta Mater. 54 (2005) 287.

[18] G.H. Bray, M. Glazov, R.J. Rioja, D. Li, R.P. Gangloff, Int. J. Fatigue, 23 (2001) 265.

[19] C. Herring, J. Appl. Phys. 21 (1950) 437.

[20] R.L. Coble, J. Appl. Phys. 34 (1963) 1679.

[21] J. Harper, J.E. Dom, Acta Metall. 5 (1957) 654.

[22] T.G. Langdon, Scripta Mater. 35 (1996) 733.

[23] R.W. Evans, B. Wilshire, Introduction to Creep, The Institute of Materials, 1993.

[24] D.M. Owen, T.G. Langdon, Mater. Sci. Engng. A, 216 (1996) 20.

[25] M.F. Ashby, Acta Mater 20 (1972) 887.

[26] M.R. Parry, S. Syngellakis, Sinclair, I., Mater. Sci. Engng. A 291 (2000) 224.

[27] Xu, Y., Gregson, P.J., Sinclair, I., Mater. Sci. Engng. A 284 (2000) 114.

[28] H. Toda, I. Sinclair, J.-Y. Buffiere, E. Maire, T. Connolley, M. Joyce, K.H. Khor and P.J. Gregson, Philosoph. Mag. 83 (2003) 2429.

[29] N. Kamp, M.R. Parry, I. Sinclair, in preparation, 2005.

Alloy 5   **Alloy 7**   **Alloy 8**
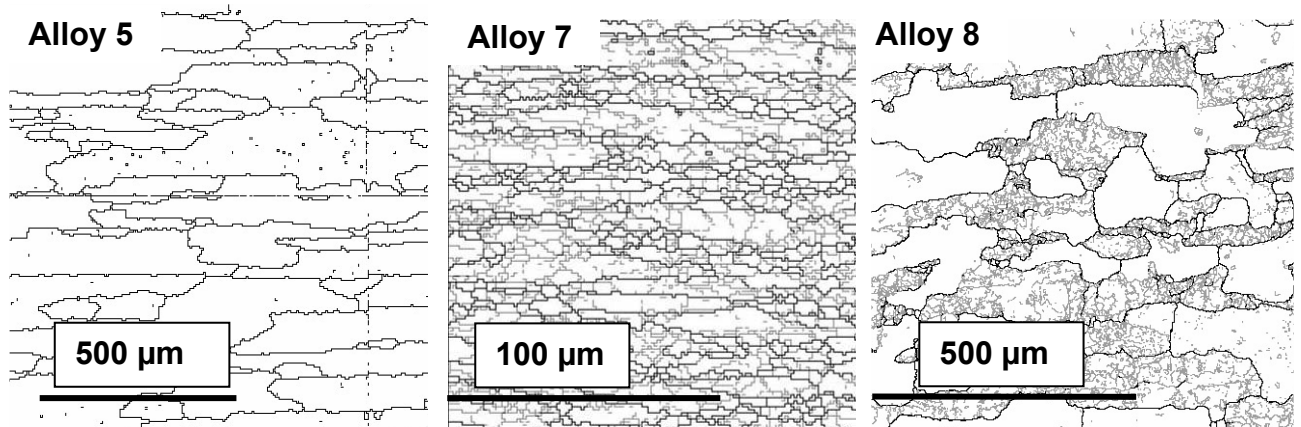
500 µm   100 µm   500 µm

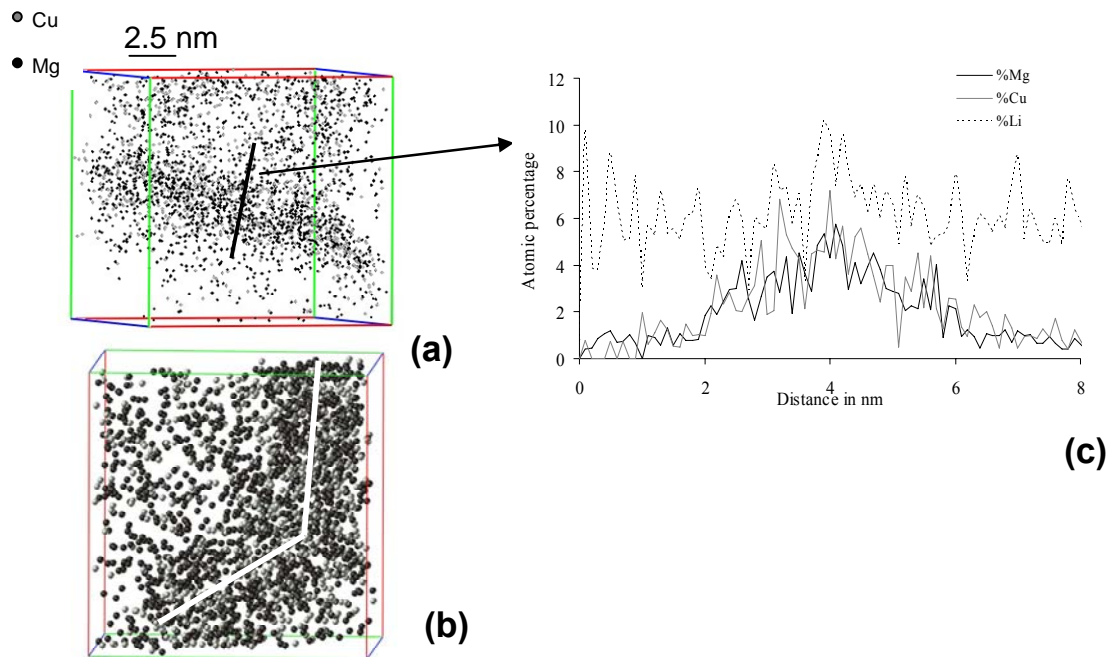Fig. 1. EBSD maps of TS face of alloys 5 (Mn-containing), 7 (Zr+Sc-containing) and 8 (Zr containing).

Fig. 2. 3DAP elemental mapping of Cu and Mg in the alloy 4 aged at 150ºC for 12h showing a precipitate: (a) side view; (b) top view with the two white lines showing the two directions of growth of the supposed merging precipitate; (c) corresponding composition profile perpendicular to the precipitate/matrix broad interface. (from Ref. [5])
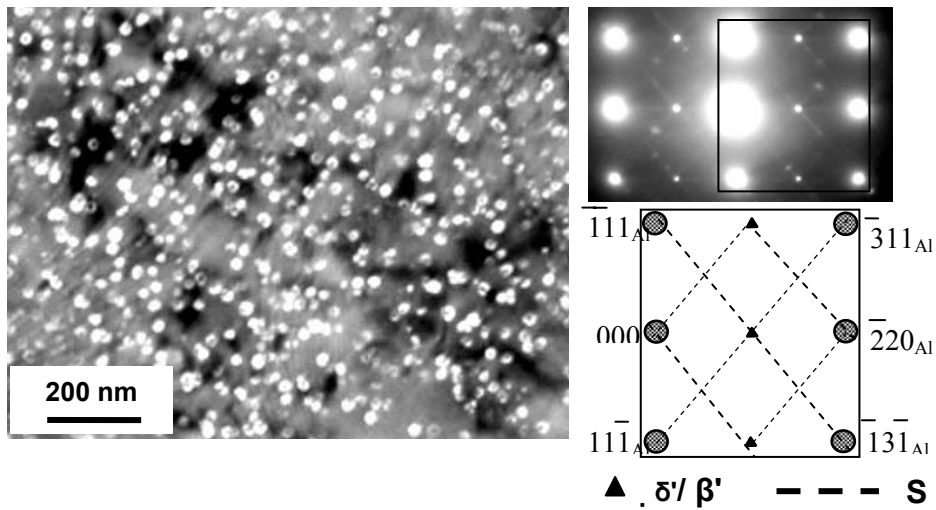
Fig. 3. TEM micrograph and selected area diffraction pattern (SADP) of the alloy 3 aged 72 h at 150°C (dark field, B=[112]) showing that many of the spherical precipitates are formed by β' (Al$_3$Zr) covered by shell of δ' (Al$_3$Li).
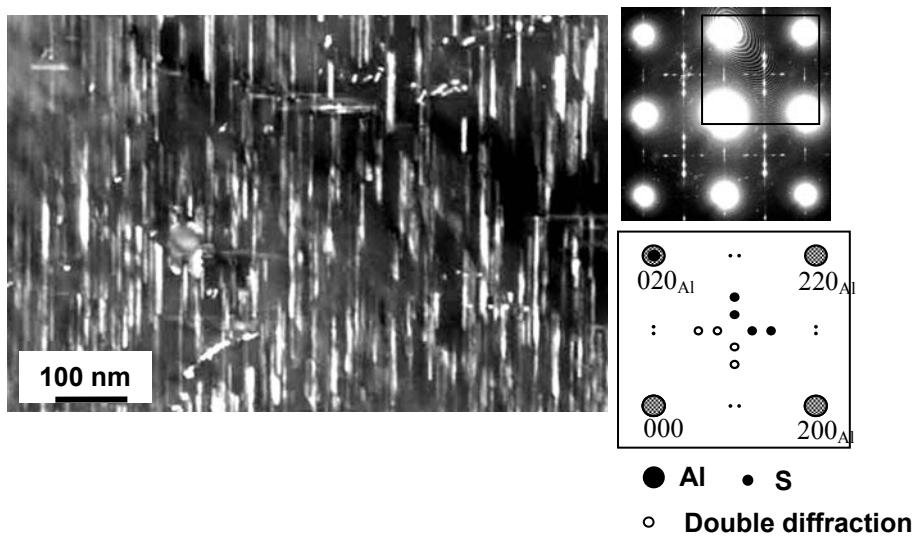
Fig. 4. TEM micrograph and SADP of the alloy 6 aged 12 h at 190°C (dark field, B=[100]) showing S precipitates.
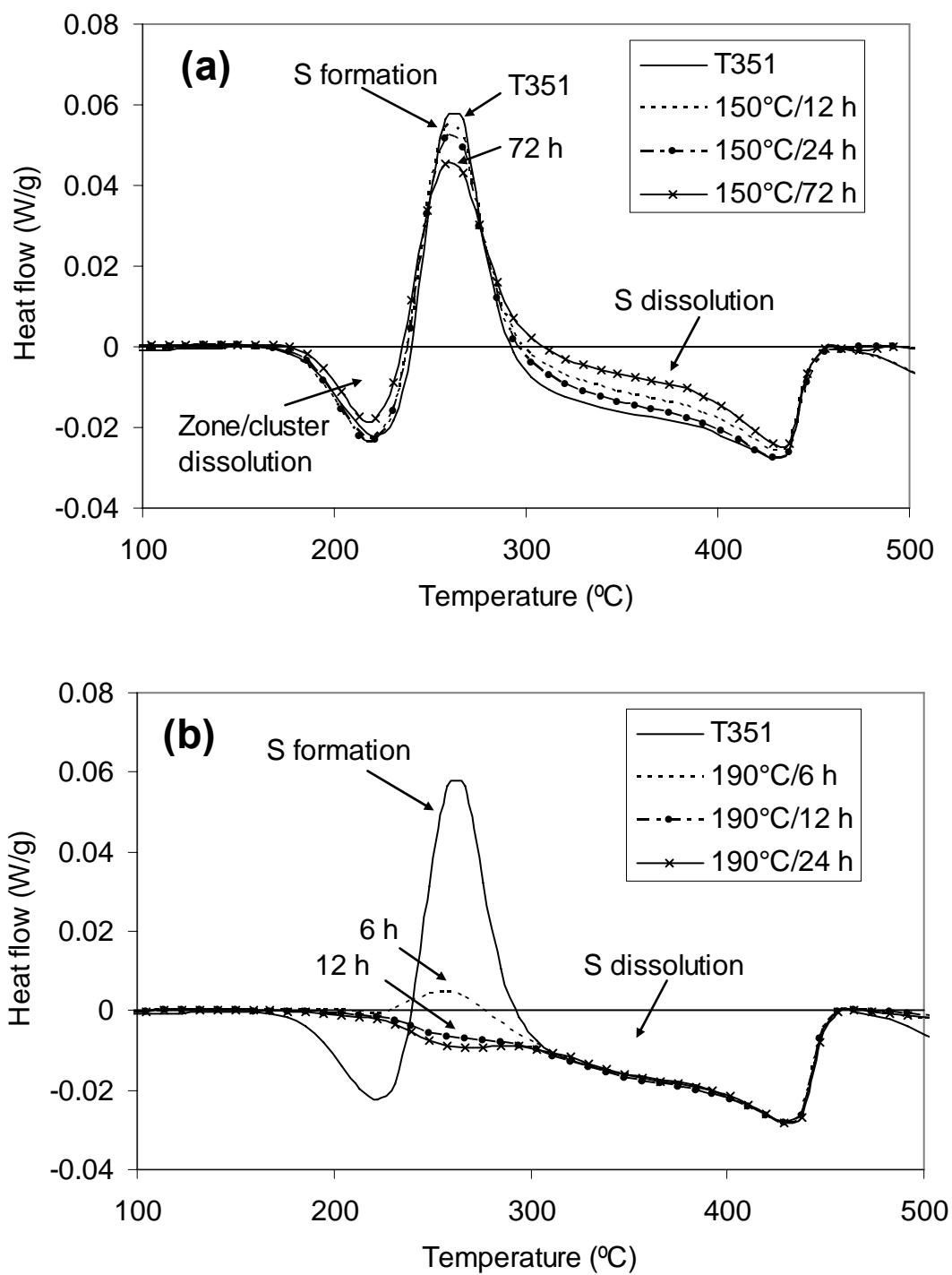
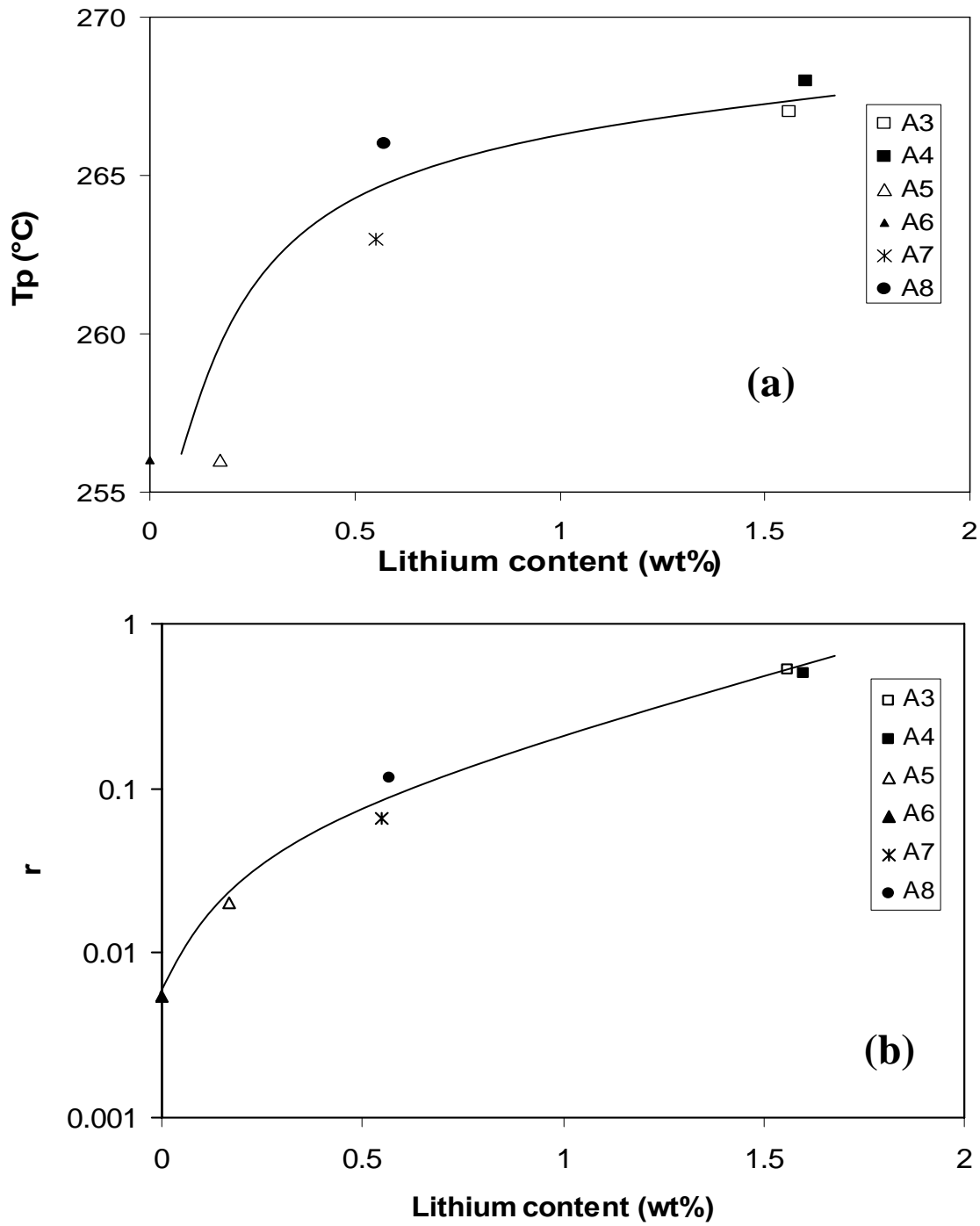Fig. 5. DSC curves of alloy 7 aged at (a) 150°C and (b) 190°C.

Fig. 6. Peak temperature of S phase formation (a) and the ratio of heat content of S phase precipitation ($r = Q_{190^\circ C/6h} / Q_{T351}$) (b) as a function of lithium content. The lines indicate general trends.
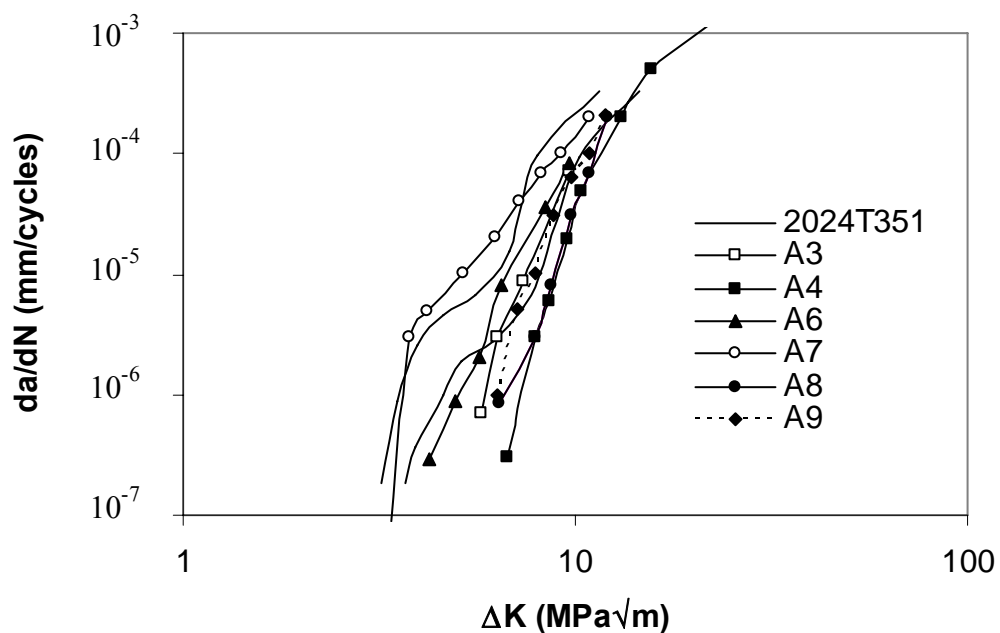
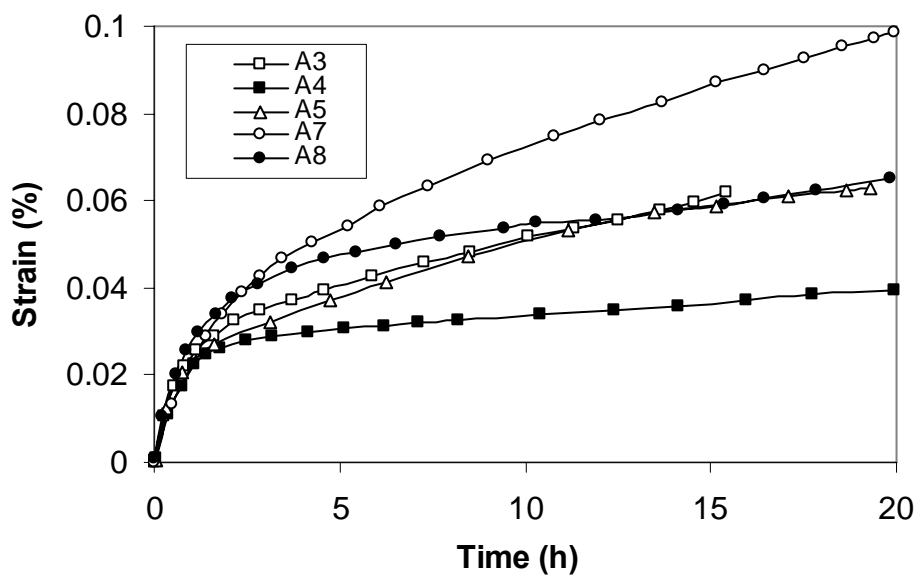Fig. 7. Fatigue crack growth results for alloys aged for 12h at 190°C.

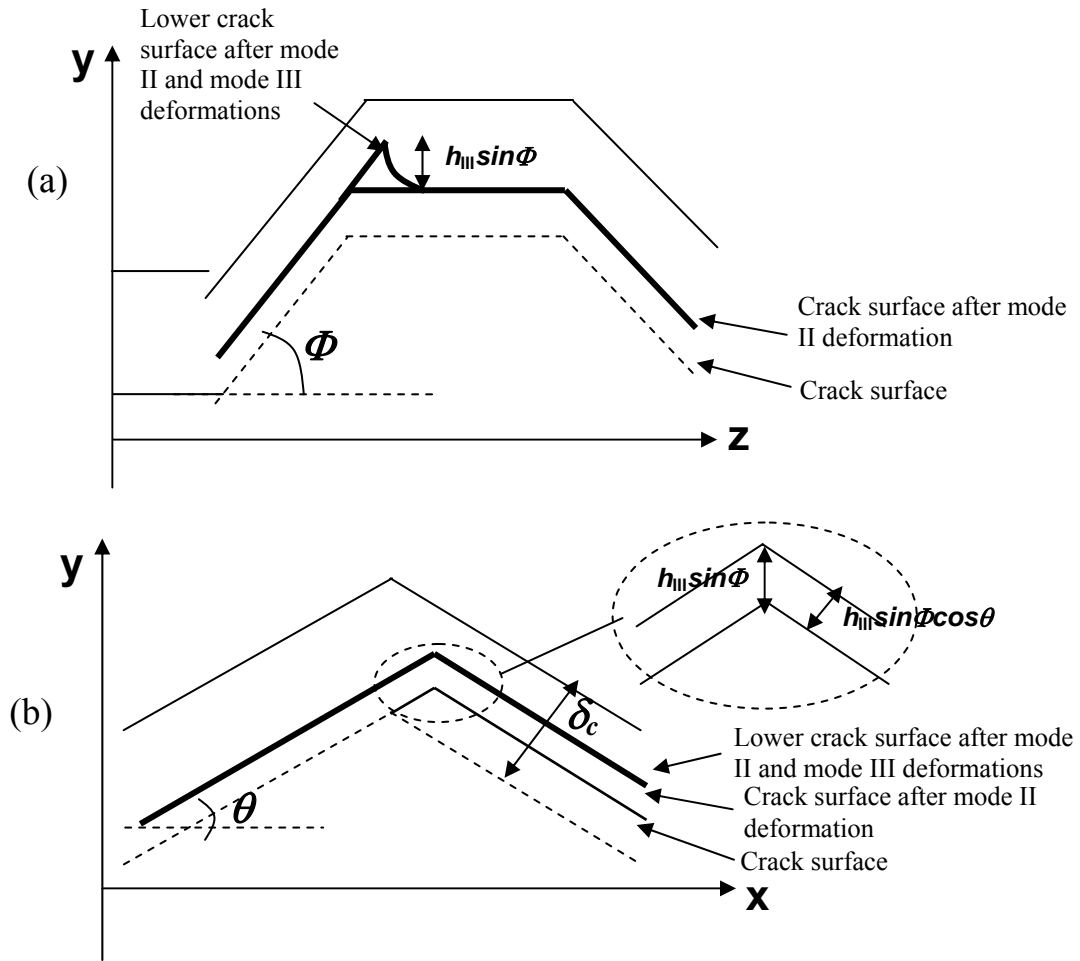Fig. 8. Creep tests results for alloys 3, 4, 5, 7, 8 at 190°C at a stress of 150MPa.

Fig. 9. Schematic illustration of the effect of mode II and mode III deformations, respectively h_{II} and h_{III}, on the formation of asperities projected along (a) the (YZ) and (b) the (YX) axes.
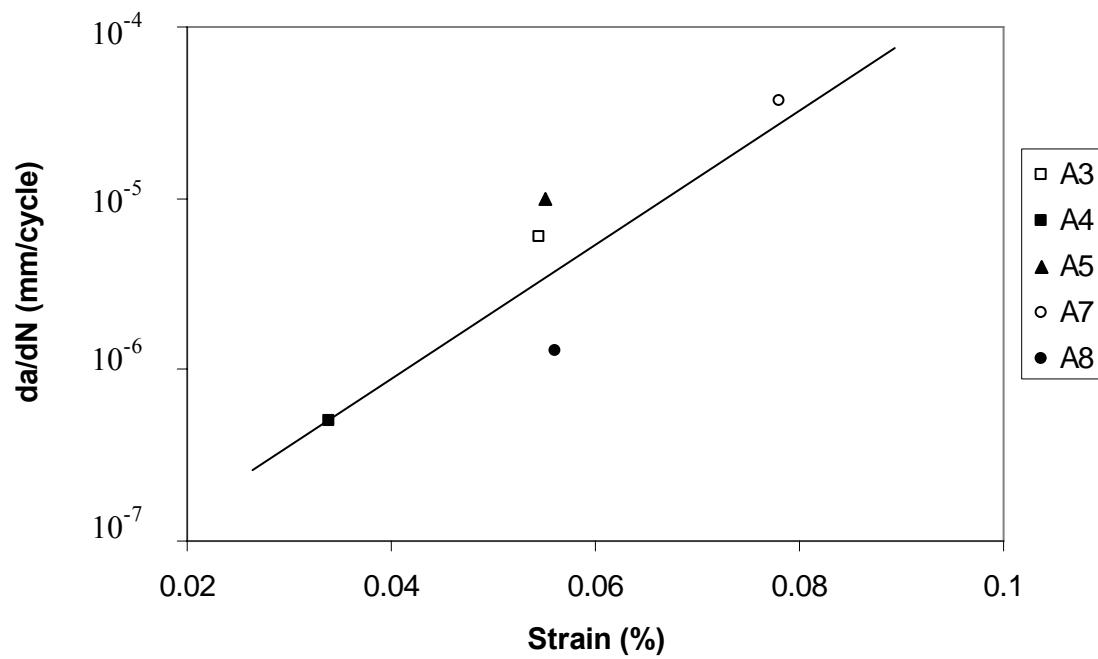
Fig. 10. The creep strain vs. the crack growth rate at $\Delta K = 7$ MPa m$^{1/2}$ for alloys with Cu content larger than 1.5 wt%.